Check for updates

Received: 8 October 2023 | Revised: 31 January 2024 | Accepted: 12 February 2024

IET Renewable Power Generation

DOI: 10.1049/rpg2.12995

The Institution of Engineering and Technology WILEY

ORIGINAL RESEARCH

Multi-mode converter control for linear generator-based wave energy system

Md Imran Ullah | **Jessica S. Döhler** | **Vinicius M. de Albuquerque** | **Johan Forslund** | **Cecilia Boström** | **Irina Temiz**

Department of Electrical Engineering, Uppsala University, Uppsala, Sweden

Correspondence
Md Imran Ullah, Department of Electrical Engineering, Uppsala University, Box 65, 75103 Uppsala, Sweden.
Email: imran.ullah@angstrom.uu.se

Funding information
Stand Up for Energy; Uppsala Universitet; Stiftelsen Åforsk, Grant/Award Number: 17-550

Abstract

The electrification of remote islands has long been a subject of research interest, primarily because of their historical reliance on fossil fuels, leading to a significant carbon footprint. Recent advancements in wave energy converters offer a promising avenue to make these islands more self-sustainable while considerably reducing carbon emissions. However, the persistent issue of voltage dips due to weaker grids continues to pose a challenge. This study introduces a multi-mode converter control strategy with the goal of electrifying remote islands, employing a linear generator-based wave energy converter in a unified electrical model. Various scenarios, including voltage dips and mainland grid disconnection, are simulated using MATLAB/Simulink. The study demonstrates the converter's ability to transition swiftly and smoothly in response to these scenarios, ensuring an uninterrupted power supply. Furthermore, the analysis indicates that the power quality at the point of common coupling remains well within acceptable standards.

1 | INTRODUCTION

Due to its technical complications and financial constraints, the electrification of islands has consistently remained a subject of research [1]. Some islands, such as Gotland in Sweden, have been integrated into the main grid [2], while others continue to rely heavily on fossil fuels [3]. The dependence on fossil fuels can lead to economic constraints due to fuel price volatility, which is susceptible to demand shifts and geopolitical factors. It also results in higher electricity costs and increased carbon emissions [4, 5].

Conversely, the adoption of renewable power sources, such as wave energy converters (WEC) for remote island's electrification, could support power stability and reduce reliance on fossil fuel and diesel generators, and potentially enhance the island's environmental profile [6–8]. Ideally, such initiatives could pave the way for these islands to achieve a level of electrical self-sufficiency.

Wave energy is a type of renewable energy transformed by the movement of ocean waves [9]. These waves are formed as a result of the continuous interaction between the wind and the ocean's surface. The potential of wave energy is staggering [10–12]. Among its many advantages, wave energy exhibits lower temporal variability compared to wind energy [13, 14] and higher average annual wave energy density(50 kW/m) [15].

Numerous technologies have emerged to convert wave energy into usable electrical energy. A few notable categories of WEC devices include point absorbers, attenuators and terminators [16]. The present study employs the WEC developed by Uppsala University [17]. It is a point absorber that should operate offshore in medium deep waters, see Figure 1.

1.1 | Challenges in the wave energy

Wave energy farm's power fluctuations are its major drawbacks [19]. Since Uppsala University's WEC has a direct drive power take-off (PTO), these variabilities can possibly be transferred to the grid [20], leading to issues such as grid instability, voltage flicker and fluctuations at the point of common coupling (PCC) [21].

On the grid side, various grid requirements must be met by electric power producers at the PCC. Each country has its own set of grid requirement codes, determined by their

This is an open access article under the terms of the Creative Commons Attribution License, which permits use, distribution and reproduction in any medium, provided the original work is properly cited.
© 2024 The Authors. *IET Renewable Power Generation* published by John Wiley & Sons Ltd on behalf of The Institution of Engineering and Technology.

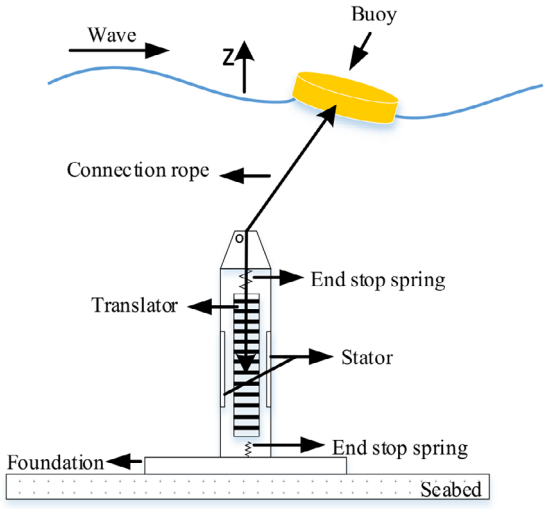

FIGURE 1 Wave energy converter [18].

respective transmission system operators (TSOs) [22]. For example, Svenska kraftnät in Sweden [23], National Grid ESO in the UK [24], and Power Grid Corporation in India [25], among others, have their specific grid connection requirements. These requirements include voltage variations, frequency variation, fault ride-through capabilities, active and reactive power control, weaker grid requirements etc. [26].

For example, ±10% of voltage variation is allowed at the PCC, as stipulated by the grid code standard IEEE 519-2022 [27]. However, for the current study, we have chosen a stricter range of ±5% voltage deviation. Additionally, the grid voltage's total harmonic distortion (THD) at the PCC must not exceed 5%, as per the IEEE 519-2022 grid code standard [27]. It is important to note that the integration of wave energy can introduce short-term voltage variations, particularly when connected to a weak grid location [28]. Consequently, further research is essential to enhance the power quality of the wave power farm.

Numerous strategies are being explored to tackle these challenges and enhance wave energy's power quality at the PCC, including use of energy storage system [29, 30], wave prediction [31], reactive power compensation [32], and WEC placement strategy [33, 34].

Energy storage systems, especially hybrid energy storage systems (HESS) are being widely studied to mitigate wave energy farm variability [35]. Various energy storage systems, such as superconducting magnetic storage system [36], battery [30], supercapacitor [37], mechanical energy storage system [38] etc. are under investigation. Energy storage systems enhance the power quality of both, individual WECs and wave farms at the PCC. Using energy storage at the DC-bus also reduces the DC-bus voltage ripple [39]. For this application, the inverter is controlled in grid-feeding (GFD) mode, supplying constant power to the grid based on the grid demand [29]. On the other hand, it also reduces the WEC power variation by charging and discharging based on the control with the help of a DC/DC converter [30].

1.2 | The need for a multimode inverter

The electrical power supply from the combined wave power farm and energy storage to a small island still presents significant challenges, mainly at the weaker grid connection point of an island [45]. Conversely, there has been an increased interest in the demand for a self-sustaining island's local power grid that can provide a steady supply of electricity to mitigate voltage dips and power outages originating from the mainland grid [46].

Voltage dips, also referred to as voltage sags, represent transient reductions in voltage magnitude that can disrupt the operation of electrical systems. These short-lived events can be caused by sudden changes in load demand within the power grid. To counteract the adverse impacts of voltage dips, inverters equipped with sophisticated grid-supporting (GS) control mechanisms offer valuable voltage support [47]. These inverters can detect the onset of a voltage dip and respond rapidly by injecting compensating currents into the grid. By doing so, they effectively boost the grid voltage during dip occurrences, helping to mitigate the negative consequences for connected loads. The swift and precise response of inverters in providing voltage support not only safeguards equipment from voltage-related disturbances but also contributes to maintaining the overall reliability and stability of the power system.

Power outages on an island can be caused by various factors. It can be due to severe weather conditions or the island's load curtailment, leading to a blackout [48]. To counteract the adverse impacts of blackouts, inverters equipped with grid-forming (GFM) control mechanisms can be used to supply the island's load with the required voltage and current at the imposed frequency [44]. In this type of control, the inverter forms the voltage and frequency at the island's PCC rather than the mainland grid.

To ensure the commercial viability of the wave energy farm, an inverter equipped with multifunctional capabilities is needed. This versatility is essential for making the wave farms grid-ready in diverse scenarios, with one notable application being the electrification of remote islands.

In previous work, only one of the control strategies, GFD or GFM, is applied, with the advantages and disadvantages summarized in Table 1. This work proposes including all three strategies (GFD, GS, and GFM) into one multi-mode inverter to remove the drawbacks of each individual strategy.

1.3 | Motivation for this work

Nevertheless, there is a lack of studies on converter controls specifically tailored for wave power farms that aim to electrify islands. Several studies have explored the effect of voltage drops and power losses at small islands when supplied from diverse energy mixes [49, 50]. Yet, these studies primarily rely on mathematical models to analyze the techno-economic aspects of island electrification using different renewable energy sources. Ref. [51] delves into the scenario of mainland grid disconnection or disturbances leading to instability in the island's electrical system. In all of these previous studies, the significance of

17521424, 0, Downloaded from https://ietresearch.onlinelibrary.wiley.com/doi/10.1049/rpg2.12995 by Uppsala University Library, Wiley Online Library on [29/04/2024]. See the Terms and Conditions (https://onlinelibrary.wiley.com/terms-and-conditions) on Wiley Online Library for rules of use; OA articles are governed by the applicable Creative Commons License

TABLE 1 Common inverter control strategies used with linear generator WECs and the proposed control method.

Ref. No.	Control type	ESS	Control features	Drawbacks
[40]	Rectification	NA	• Smoother dc voltage	• Not grid-connected • Varying frequency of the WEC output voltage and current • Varying amplitude of the WEC output voltage and current
[39, 41]	GFD	NA	• Grid connected • Inverter regulates the dc voltage	• Fluctuating power • Higher grid voltage and current THD
[42]	GFD	HESS	• Constant power to the grid • HESS regulates the dc voltage	• Off-grid application not available
[43]	GFM	Battery and Supercapacitor	• Island electrification	• Limited to only off-grid loads • Energy storage used in multiple locations
[44]	GFM	HESS	• Island electrification	• Not grid-connected
Proposed control	Combination of GFD GS GFM	HESS	• Constant power to the island and the grid • Island's voltage dips rectified • Voltage and frequency are formed at the island in the event of mainland grid disconnection • The control transitions between these modes enabling island's electricity autonomy	• Increased complexity of the control

comprehensive converter control investigations for practical implementation is emphasized, which is the focus of this paper.

In a separate study, ref. [43] utilizes wave energy to supply an off-grid residential load through grid-forming inverter control. However, ref. [43] does not address the scenario of mainland grid connection or the potential impact of voltage drops. Hence, the need for a smart inverter that bypasses voltage dips and maintains acceptable power quality is vital for a wave energy farm supplying an island.

In light of this context, the present paper introduces a multimode control approach for a grid-side inverter, enabling the provision of consistent power from the wave energy converter to a remote island, which can be seen in Figure 2. A three-phase reactive load is used to represent an island's load. Three distinct control modes have been implemented using MATLAB/Simulink:

- GFD: In this mode, the grid-side inverter regulates the power supplied to the grid based on active and reactive power control methods [52]. The mainland grid is connected to the offshore grid bus in this scenario.
- GS: This mode aims to assist the grid in amending the voltage drops occurring at the PCC [47].
- GFM: This mode enables the island to function as an independent power system. It is activated when the mainland grid connection is lost. Here, the inverter, with the aid of wave energy and energy storage, generates voltage and frequency at the PCC [53].

The paper employs a single inverter across three distinct modes, determined by the state of the mainland grid connection. Notably, the control system highlights seamless and rapid transitions between these modes. This study employs an innovative methodology by incorporating the wave power farm PTO system into a unified electrical model. This integrated model enables a comprehensive examination of wave power farm grid integration, encompassing the intricate dynamics of multiple converters, the DC-bus, and the grid at a higher level of granularity. Additionally, an analysis of THD is conducted for both three-phase voltage and current at the PCC to showcase the power quality of the wave power farm. This study considers a strong mainland grid.

The remaining paper is organized as follows:

- Section 2 is divided into four parts describing the methodology applied in the study. This section describes the WEC, system description, mathematical modelling and control of multimode inverter and hybrid energy storage system control.
- Section 3 goes through the simulation setup.
- Section 4 presents and discusses the simulated results.
- Section 5 concludes the work and summarizes the findings.

2 | METHODOLOGY

2.1 | Wave energy converter

The WEC used in this study is Uppsala University's wave energy converter. It can also be seen in Figure 1. It uses a permanent magnet non-salient synchronous generator. The generator consists of a wounded stator and a permanent magnet-mounted translator [54]. The generator is put down on the sea bed. A

17521424, 0, Downloaded from https://ietresearch.onlinelibrary.wiley.com/doi/10.1049/rpg2.12995 by Uppsala University Library, Wiley Online Library on [29/04/2024]. See the Terms and Conditions (https://onlinelibrary.wiley.com/terms-and-conditions) on Wiley Online Library for rules of use; OA articles are governed by the applicable Creative Commons License

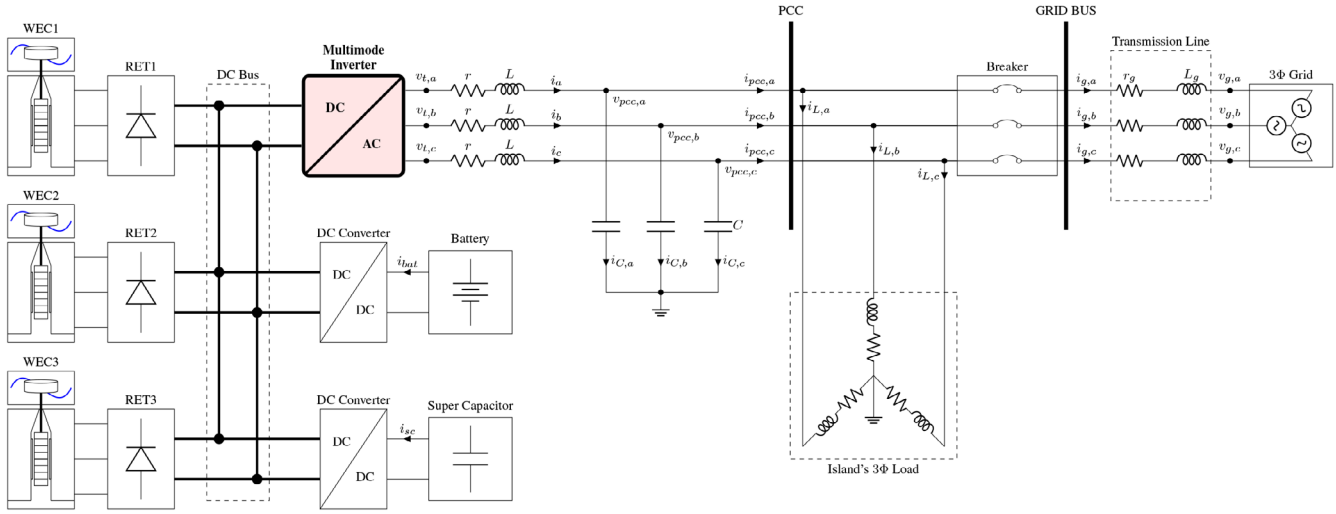

FIGURE 2 Block diagram of the proposed wave energy electrical network.

floating buoy is connected to the generator's translator through a connection rope. The translator is lifted by the heave motion of the buoy and gravitational forces bring it down to the sea bed.

The movement between the buoy and the translator can either make the connection line tight or slack. The connection line slacks when the displacement of the buoy can be greater than that of the translator's displacement. This model uses a slack connection for the WEC system. According to Newton's second law of motion, two distinct equations governing the motion of the translator and the buoy are given correspondingly [55]:

$$m_{\mathrm{B}}\ddot{\vec{z}}_{\mathrm{B}}(t) = \vec{F}_{\mathrm{GB}} + \vec{F}_{\mathrm{WB}}(t) + \vec{F}_{\mathrm{B}} + \vec{F}_{\mathrm{E}}(t) + \vec{F}_{\mathrm{R}}(t) + \vec{F}_{\mathrm{HS}}(t) \quad (1)$$

and

$$m_{\mathrm{T}}\ddot{\vec{z}}_{\mathrm{T}}(t) = \vec{F}_{\mathrm{GT}} + \vec{F}_{\mathrm{PTO}}(t) + \vec{F}_{\mathrm{WT}}(t) + \vec{F}_{\mathrm{ES}}(t), \quad (2)$$

where m_{B}, m_{T} are the mass of the buoy and translator; $\ddot{\vec{z}}_{\mathrm{B}}(t)$, $\ddot{\vec{z}}_{\mathrm{T}}(t)$ are the accelerations of the buoy and translator correspondingly; $\vec{F}_{\mathrm{GB}}$, $\vec{F}_{\mathrm{GT}}$ are the gravitational forces on the buoy and translator; $\vec{F}_{\mathrm{B}}$ is the buoyancy force; $\vec{F}_{\mathrm{E}}(t)$ is the excitation force; $\vec{F}_{\mathrm{R}}(t)$ is the radiation force; $\vec{F}_{\mathrm{HS}}(t)$ is the hydrostatic restoring force; $\vec{F}_{\mathrm{PTO}}(t)$ is the damping force of the PTO; $\vec{F}_{\mathrm{ES}}(t)$ is the end-stop force; $\vec{F}_{\mathrm{WB}}(t)$ and $\vec{F}_{\mathrm{WT}}(t)$ are the wire force for the buoy and the translator, respectively. The forces acting on the buoy and translator can be seen in Figure 3. The reader can refer to [55] and [18] for the detailed modelling of the different forces.

Assuming cosinusoidal magnetic flux, the magnetic flux in the stator windings is given by

$$\Phi = \Phi_0 \cos\left(\frac{2\pi}{\tau_{\mathrm{p}}} z_{\mathrm{t}}(t) + \psi\right) \quad (3)$$

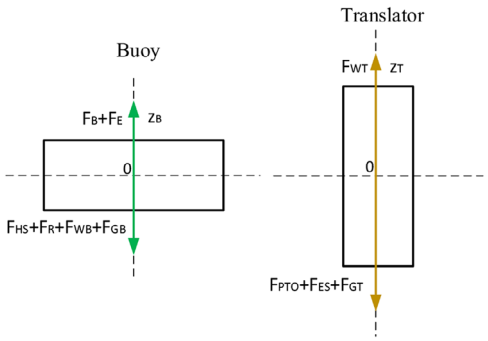

FIGURE 3 Forces acting on the buoy and the translator [18].

where Φ_0 is the amplitude of the magnetic flux, τ_{p} is the pole pair width, $z_{\mathrm{t}}(t)$ is the translator displacement, and ψ is the phase shift, $\psi = 0, \pm 2\pi/3$.

The generator-induced EMF e is calculated from

$$e = -N\frac{\mathrm{d}\Phi}{\mathrm{d}t} = E_{\mathrm{p}} \sin\left(\frac{2\pi}{\tau_{\mathrm{p}}} z_{\mathrm{t}}(t) + \psi\right) \quad (4)$$

where $E_{\mathrm{p}} = 2\pi N \Phi_0 \dot{z}_{\mathrm{t}}/\tau_{\mathrm{p}}$ is the amplitude of no-load voltage, and N is the total number of turns of the stator windings.

The WEC PTO model is subjected to excitation force as an input parameter. The excitation force used for the current study is from an irregular wave. The reader can refer to [54] and [56] for the detailed modelling of the WECs linear generator.

2.2 | System description

This subsection outlines the proposed electrical layout of the wave energy farm and the energy storage which is electrifying a remote island. The objective is to provide electricity to an offshore island, represented in this context as a three-phase load, as illustrated in Figure 2.

17521424, 0, Downloaded from https://ietresearch.onlinelibrary.wiley.com/doi/10.1049/rpg2.12995 by Uppsala University Library, Wiley Online Library on [29/04/2024]. See the Terms and Conditions (https://onlinelibrary.wiley.com/terms-and-conditions) on Wiley Online Library for rules of use; OA articles are governed by the applicable Creative Commons License

The proposed system involves a wave energy farm supplying power to a remote island, which, in turn, is connected to the utility grid. The wave farm comprises three WECs, each subjected to the same wave excitation force. However, It is important to note that the energy aggregation effect within the wave power farm is obtained by random shift of the excitation forces for each WEC. These time shifts reflect the relative proximity of the three WECs and contribute to the formation of a farm structure. The proposed technology involves the deployment of farms comprising several WECs to achieve the necessary power rating. However, for the current study, we have chosen to use only three WECs to minimize computational requirements and place greater emphasis on exploring power electronics control aspects.

Each WEC system is linked to the DC-bus via a generator-side converter. The generator-side converter is a three-phase diode-based passive rectifier. Additionally, a hybrid energy storage system is connected to the DC-bus through a non-isolated bi-directional DC/DC converter. This hybrid energy storage comprises a battery and a supercapacitor. The battery is responsible for low-frequency wave power fluctuation whereas the supercapacitor is responsible for the higher-frequency fluctuations.

The three-phase load, symbolizing a remote island, connects to the PCC through a three-phase IGBT-based 2-L inverter and an RLC filter. Furthermore, the three-phase load is interconnected with the utility grid via an RL filter at the grid connection bus bar. A three-phase circuit breaker is employed for the purpose of disconnecting the mainland utility grid in the event of a grid-isolated scenario.

2.3 | Mathematical modelling and control of the multi-mode inverter

Figure 2 depicts the multi-mode inverter connected to a distribution network through a first-order low-pass passive filter. The parameters r, L, and C represent the resistance, inductance, and capacitance of the interface filter, respectively. The distribution network is modelled by the equivalent resistance r_π and inductance L_π, which are series-connected to an ideal three-phase source. In this work, it is assumed that the network voltages are balanced with only the positive-sequence component.

2.3.1 | Current control loops for the grid side inverter

The mathematical modelling of the circuit shown in Figure 2, enables the formulation of the following equations for the terminal currents of the converter:

$$\begin{cases} L\dfrac{\mathrm{d}i_a(t)}{\mathrm{d}t} = v_{\mathrm{t},a}(t) - ri_a(t) - v_{\mathrm{pcc},a}(t) \\ L\dfrac{\mathrm{d}i_b(t)}{\mathrm{d}t} = v_{\mathrm{t},b}(t) - ri_b(t) - v_{\mathrm{pcc},b}(t) \\ L\dfrac{\mathrm{d}i_c(t)}{\mathrm{d}t} = v_{\mathrm{t},c}(t) - ri_c(t) - v_{\mathrm{pcc},c}(t), \end{cases} \tag{5}$$

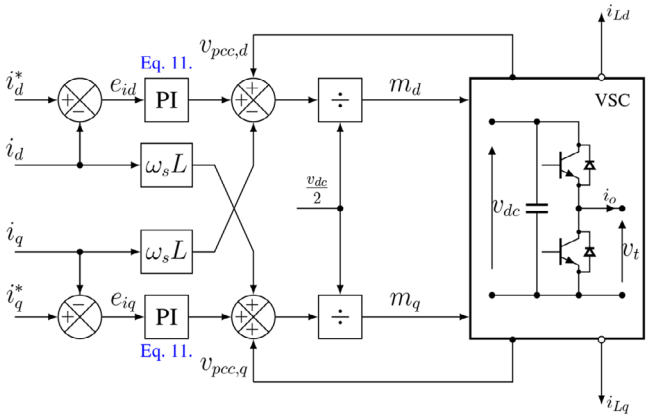

FIGURE 4 Current control loop block for the inverter, in the *dq*-frame using feed-forward decoupling.

where $v_{\mathrm{pcc},a}(t)$, $v_{\mathrm{pcc},b}(t)$, and $v_{\mathrm{pcc},c}(t)$ are the three-phase voltages at PCC, $v_{\mathrm{t},a}(t)$, $v_{\mathrm{t},b}(t)$, and $v_{\mathrm{t},c}(t)$ are the voltages in the terminal at the converter terminals. The current balance equations across the output filter are based on a synchronous reference frame system (*dq*-frame), as given by:

$$\begin{cases} L\dfrac{\mathrm{d}i_d(t)}{\mathrm{d}t} = L\omega_{\mathrm{s}}i_q(t) + v_{\mathrm{t},d}(t) - ri_d(t) - v_{\mathrm{pcc},d}(t) \\ L\dfrac{\mathrm{d}i_q(t)}{\mathrm{d}t} = -L\omega_{\mathrm{s}}i_d(t) + v_{\mathrm{t},q}(t) - ri_q(t) - v_{\mathrm{pcc},q}(t). \end{cases} \tag{6}$$

The subscripts d and q represent the d-and q-axis components of the corresponding variables. Due to the transformation to the synchronously rotating reference frame, cross-coupling between the direct-axis and quadrature-axis currents emerges, represented by the terms $\omega_{\mathrm{s}}i_q(t)$ and $\omega_{\mathrm{s}}i_d(t)$. Synchronizing a system through an inverter connected to the grid using a phase-locked loop (PLL) is a fundamental technique for achieving seamless integration of distributed energy resources. The PLL serves as a sophisticated control mechanism that ensures precise alignment between the inverter's output and the grid's voltage and frequency. The utilization of sinusoidal pulse width modulation (SPWM) within the inverter *dq* current loop enhances control precision by efficiently regulating the currents in the rotating reference frame. Thus, the system described by Equation (6) is rewritten as follows

$$\begin{cases} m_d(t) = \dfrac{2}{V_{\mathrm{cc}}(t)}\left(u_d(t) - L\omega_{\mathrm{s}}i_q(t) + v_{\mathrm{pcc},d}(t)\right) \\ m_q(t) = \dfrac{2}{V_{\mathrm{cc}}(t)}\left(u_q(t) + L\omega_{\mathrm{s}}i_d(t) + v_{\mathrm{pcc},q}(t)\right), \end{cases} \tag{7}$$

where m_d and m_q represent the direct-axis and quadrature modulation indices, respectively, while $u_d(t)$ and $u_q(t)$ are the new control variables in the system. Figure 4 shows the simplified block diagram of the control loop used to regulate the currents i_d and i_q.

The feedback control loop of the current control, which has a plant

$$P(s) = \frac{1}{Ls + r}, \tag{8}$$

17521424, 0, Downloaded from https://ietresearch.onlinelibrary.wiley.com/doi/10.1049/rpg2.12995 by Uppsala University Library, Wiley Online Library on [29/04/2024]. See the Terms and Conditions (https://onlinelibrary.wiley.com/terms-and-conditions) on Wiley Online Library for rules of use; OA articles are governed by the applicable Creative Commons License

when combined with a PI controller, it assumes a critical role in the current loop control of an inverter, facilitating the precise and stable regulation of currents to their desired values. The PI's transfer function can be written

$$C_d(s) = C_q(s) = k_{p,i}\frac{s + \frac{k_{i,i}}{k_{p,i}}}{s}. \tag{9}$$

The equation of the closed loop is compared with the first-order equation

$$F(s) = \frac{1}{\tau_i s + 1}, \tag{10}$$

in order to find the control gains

$$\begin{aligned} k_{p,i} &= \frac{L}{\tau_i} \quad \text{and} \\ k_{i,i} &= \frac{r}{\tau_i}. \end{aligned} \tag{11}$$

A recommended range of τ_i lies between 0.5 and 5 ms according to [52]. We have chosen to adopt 0.5 ms.

2.3.2 | Voltage control loop for the grid side inverter

Within this system, two distinct voltage control loops are implemented, each serving a specific purpose based on the operational context. The first voltage control loop operates when the system is grid-connected, aiming to provide voltage support to the existing grid. This loop ensures that the system's output voltage aligns with the nominal grid voltage, contributing to the stability of the system. In contrast, the second voltage control loop comes into play when the system operates in isolation from the grid, generating its own voltage and frequency reference. In this scenario, the control loop works to maintain the generated voltage and frequency at the desired levels, enabling the system to function autonomously while adhering to predetermined operating parameters. This dual-voltage control strategy underscores the adaptability of the multi-mode inverter functionality, allowing it to seamlessly transition between grid-connected support and standalone voltage and frequency generation modes.

Grid-connected island scenario:

To establish a comprehensive grid model applicable to balanced scenarios, the configuration depicted in Figure 5 is adopted. The grid's representation is derived by formulating the voltage equation between the reference points at the V_{pcc} (PCC) and V_{g} (utility grid) [47, 57].

The following equation represents the voltage relationship between referenced points

$$\vec{v}_{\text{pcc}}(t) = r_{\text{g}}\,\vec{i}_{\text{g}}(t) + L_{\text{g}}\frac{\mathrm{d}\vec{i}_{\text{g}}}{\mathrm{d}t} + j\omega L_{\text{g}}\vec{i}_{\text{g}}(t) + \vec{v}_{\text{g}}(t). \tag{12}$$

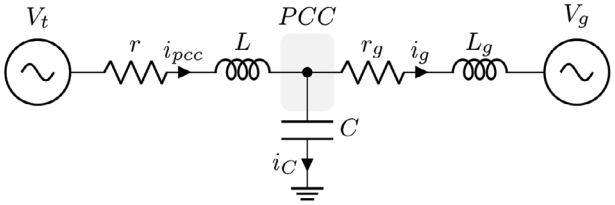

FIGURE 5 Unifilar diagram of the voltage compensation at the PCC.

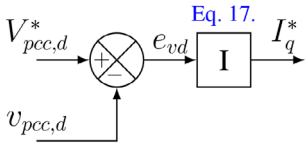

FIGURE 6 Voltage support control block diagram.

The grid filter is not taken into account to obtain such a model, since PCC voltage variations in an unbalanced system are imposed by the grid impedance and not by the grid filter. The grid model is expressed as a double *dq* synchronous reference frame

$$\begin{cases} v_{\text{pcc},d}(t) \approx L_{\text{g}}\frac{\mathrm{d}i_{\text{g},d}(t)}{\mathrm{d}t} - \omega L_{\text{g}} i_{\text{g},q}(t) + r_{\text{g}} i_{\text{g},d}(t) + v_{\text{g},d}(t) \\ v_{\text{pcc},q}(t) \approx L_{\text{g}}\frac{\mathrm{d}i_{\text{g},q}(t)}{\mathrm{d}t} + \omega L_{\text{g}} i_{\text{g},d}(t) + r_{\text{g}} i_{\text{g},q}(t) + v_{\text{g},q}(t). \end{cases} \tag{13}$$

The voltage amplitude $v_{\text{pcc},d}(t)$ can be controlled using the currents $i_{\text{g},d}(t)$ and $i_{\text{g},q}(t)$ in the *dq* synchronous coordinate system. However, as the network resistance r_π is considered very small, its contribution to the PCC voltage can be neglected since the network impedance is considered to be inductive. In this type of application, the current component $i_{\text{g},q}(t)$ controls the voltage $v_{\text{pcc},d}(t)$. It is also observed that the PLL guarantees the voltage $v_{\text{pcc},q}(t)$ in the *d*-axis direction. Figure 6 depicts the voltage support control block diagram.

The voltage can be controlled with an integral (I) controller,

$$C_{v,q}(s) = \frac{k_{i,vs}}{s}. \tag{14}$$

The plant model of the PCC is $G_q(s) = L_\pi$, and the closed-loop transfer function is given by

$$H(s) = \frac{V^*_{\text{pcc},d}}{v_{\text{pcc},d}} = \frac{C_{v,q}(s)G_q(s)}{1 + C_{v,q}(s)G_q(s)}. \tag{15}$$

Comparing the equation $H(s)$ with the first-order canonical

$$M(s) = \frac{1}{1 + \tau_v s}, \tag{16}$$

the gain can be written

$$k_{i,vs} = \frac{1}{\tau_v \omega_s L_\pi}. \tag{17}$$

17521424, 0, Downloaded from https://ietresearch.onlinelibrary.wiley.com/doi/10.1049/rpg2.12995 by Uppsala University Library, Wiley Online Library on [29/04/2024]. See the Terms and Conditions (https://onlinelibrary.wiley.com/terms-and-conditions) on Wiley Online Library for rules of use; OA articles are governed by the applicable Creative Commons License

Assuming that the time constant of the closed-loop transfer function of the quadrature-axis positive-sequence current (τ_i) is substantially smaller than the time constant (τ_v) of the direct-axis voltage closed-loop transfer function, the integrator gain can be calculated by making $\tau_v \geq 10\tau_i$, which results in a good current signal filtering [47].

Grid-isolated island scenario:
The necessity to use a converter when a system is isolated from the grid arises from the fundamental need to maintain essential electrical parameters such as voltage and frequency within acceptable limits. In a standalone system, there may be fluctuations in both voltage and frequency due to variations in load demand or the inherent characteristics of renewable energy sources like waves. A converter, often in the form of an inverter, can regulate and stabilize the output voltage and frequency to match the required grid standards or meet the specific needs of connected loads.

The equations for the terminal of the output LC filter in Figure 2 follows:

$$\begin{cases} C\dfrac{\mathrm{d}v_{\mathrm{pcc},a}(t)}{\mathrm{d}t} = i_a(t) - i_{\mathrm{L},a}(t) \\ C\dfrac{\mathrm{d}v_{\mathrm{pcc},b}(t)}{\mathrm{d}t} = i_b(t) - i_{\mathrm{L},b}(t) \\ C\dfrac{\mathrm{d}v_{\mathrm{pcc},c}(t)}{\mathrm{d}t} = i_c(t) - i_{\mathrm{L},c}(t), \end{cases} \tag{18}$$

where $i_{\mathrm{L},a}(t)$, $i_{\mathrm{L},b}(t)$, and $i_{\mathrm{L},c}(t)$ are the three-phase current of the load. The voltage equations across the output filter are based on a *dq*-frame, as given by

$$\begin{cases} C\dfrac{\mathrm{d}v_{\mathrm{pcc},d}(t)}{\mathrm{d}t} = C\omega_{\mathrm{s}}v_{\mathrm{pcc},q}(t) + i_d(t) - i_{\mathrm{L},d}(t) \\ C\dfrac{\mathrm{d}v_{\mathrm{pcc},q}(t)}{\mathrm{d}t} = -C\omega_{\mathrm{s}}v_{\mathrm{pcc},d}(t) + i_q(t) - i_{\mathrm{L},q}(t). \end{cases} \tag{19}$$

Once the synchronous reference frame control converts the three-phase voltage and current variables into *dq* signals [52], the cascade control strategy is used. This strategy employs two PI controllers, with the ac voltage controller's output serving as the reference for the ac current controller described in the Section 2.3.1. Notably, the feedback loop for one controller is nested within the other, creating an interconnected structure as illustrated in Figure 7.

The reference values $V^*_{\mathrm{pcc},d}$ and $V^*_{\mathrm{pcc},q}$ define the magnitude regulation whereas frequency can be set by choosing an internal value for ω_{s}. The feedback control loop of the voltage control, which has a plant

$$V(s) = \frac{1}{Cs} \tag{20}$$

is combined with a PI controller

$$C_{vd}(s) = C_{vq}(s) = k_{p,v}\frac{s + \frac{k_{i,v}}{k_{p,v}}}{s} \tag{21}$$

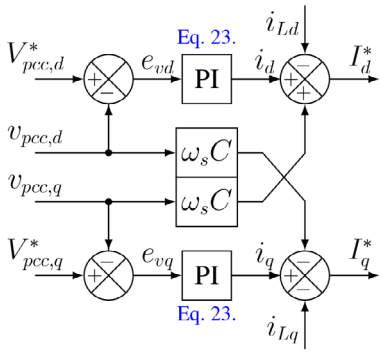

FIGURE 7 Block diagram of the grid forming inverter control that generates the reference currents in the *dq*-frame.

TABLE 2 Parameters of the multi-mode inverter.

Parameter	Value
Nominal voltage (V_{rms})	220 V
Switching frequency	24 kHz
Nominal frequency	50 Hz
LC filter	$r_\pi = 0.3\ \Omega$, $L_\pi = 2$ mH and $C = 90\ \mu$F
Line impedance	$r_g = 0.16\ \Omega$ and $L_g = 2$ mH
Nominal dc voltage	600 V
DC-Bus capacitor	$C_{eq} = 5500\ \mu$F
Current loop gains	$k_{p,i} = 4.8$ and $k_{i,i} = 720$
Voltage loop gains isolated	$k_{p,v} = 0.1728$ and $k_{i,v} = 169.27$
Voltage loop gains connected	$k_{i,v} = 106.10$

The equation of the closed loop is compared with the second-order equation

$$G(s) = \frac{2\xi\omega_n s + \omega_n^2}{s^2 + 2\xi\omega_n s + \omega_n^2} \tag{22}$$

in order to find the gains of the control, resulting in

$$\begin{aligned} k_{p,v} &= C\omega_n^2 \\ k_{i,v} &= 2C\xi\omega_n. \end{aligned} \tag{23}$$

For natural frequency $\omega_n = 2\pi \times 182$ rad/s and the damping ratio $\xi = 0.707$. The parameters multi-mode inverter and the control loop gains are given in Table 2.

2.4 | Hybrid energy storage system control

A HESS is employed in the current study to mitigate wave power farm variability and maintain stable DC-bus voltage. The HESS comprises a battery and supercapacitor in the current case. Specifically, the battery handles low-frequency fluctuations originating from the WEC farm, while the

17521424, 0, Downloaded from https://ietresearch.onlinelibrary.wiley.com/doi/10.1049/rpg2.12995 by Uppsala University Library, Wiley Online Library on [29/04/2024]. See the Terms and Conditions (https://onlinelibrary.wiley.com/terms-and-conditions) on Wiley Online Library for rules of use; OA articles are governed by the applicable Creative Commons License

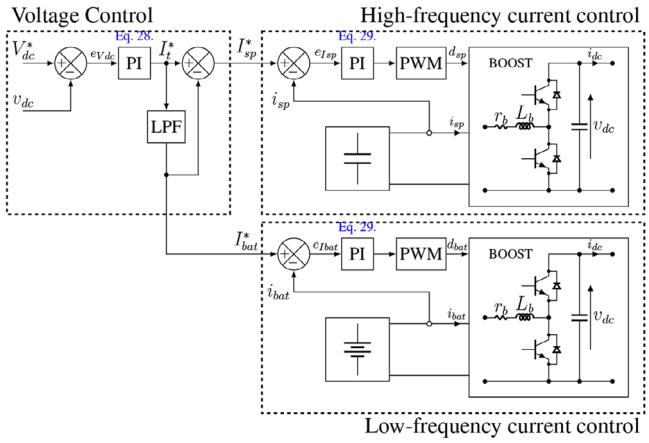

FIGURE 8 Block diagram of voltage and current control for HESS.

supercapacitor addresses high-frequency fluctuations. This division of responsibilities is due to the supercapacitor's higher power density compared to the battery, giving it an advantage during high-power charging and discharging [58].

However, the incorporation of a HESS increases system complexity and necessitates the implementation of an energy management system. The energy management system is used to accurately distribute power among the various energy storage components while maintaining the DC-bus voltage at the required level. The battery and supercapacitor are interconnected via non-isolated bidirectional DC/DC converters, facilitating the charging and discharging of the energy storage systems in accordance with the control requirements. Figure 8 illustrates the control strategy implemented within the HESS.

2.4.1 | Voltage control loop for the hybrid energy storage converter

The DC-bus voltage (v_{dc}) is controlled by the voltage control loop. The error signal from the DC-bus voltage is sent to the PI controller which generates the reference for the supercapacitor's inner current control loop. The block diagram for voltage and current control can be seen in Figure 8. Kirchhoff's current law is used to derive the outer voltage control loop which results in the following differential equation

$$i_{\mathrm{sp}}(t) = i_{\mathrm{dc}}(t) + \frac{C_{\mathrm{eq}} v_{\mathrm{dc}}(t)}{\mathrm{d}t}. \tag{24}$$

The voltage control feedback loop, represented by a plant

$$D(s) = \frac{1}{C_{\mathrm{eq}} s}, \tag{25}$$

is integrated with a PI controller

$$C_v(s) = k_{p,\mathrm{vdc}} \frac{s + \frac{k_{i,\mathrm{vdc}}}{k_{p,\mathrm{vdc}}}}{s}. \tag{26}$$

This results in a closed-loop equation, which can be compared to a second-order equation

$$C_v(s) = k_{p,\mathrm{vdc}} \frac{s + \frac{k_{i,\mathrm{vdc}}}{k_{p,\mathrm{vdc}}}}{s} \tag{27}$$

to find the gains of the PI controller, which are

$$\begin{aligned} k_{p,\mathrm{vdc}} &= 2\xi_{\mathrm{dc}} \omega_{n\mathrm{dc}} C_{\mathrm{eq}} \\ k_{i,\mathrm{vdc}} &= \omega_{n\mathrm{dc}}^2 C_{\mathrm{eq}}, \end{aligned} \tag{28}$$

where $\omega_{n\mathrm{dc}} = 2\pi \times 128$ rad/s and $\xi_{\mathrm{dc}} = 0.707$.

2.4.2 | Current control loop for the hybrid energy storage converter

The control loop for the supercapacitor follows a similar modelling approach as that of a battery. In the equations, the letters 'm' and 'n' represent the battery and supercapacitor, respectively. From Figure 8, Kirchhoff's voltage law is used to establish the voltages in the internal control loop, which results in the following differential equation

$$L_{m,n} \frac{\mathrm{d}i_{m,n}(t)}{\mathrm{d}t} + r_{m,n} i_{m,n}(t) = v_{m,n}(t) - v_{t_{m,n}}(t), \tag{29}$$

where $v_{t_{m,n}}(t)$ represents the terminal voltage, $v_{m,n}(t)$, denotes the voltage across the battery and supercapacitor, $i_{m,n}(t)$ stands for the current flowing through the battery and supercapacitor, $L_{m,n}(t)$ is the inductor filter and $r_{m,n}$ is the internal resistance of the filter. The converter uses pulse-width modulation (PWM) as its control strategy, given the relation $v_{t_{m,n}} = d_{m,n}(t)\, v_{\mathrm{dc}}(t)$.

As stated by the internal model principle, a proportional-integral controller is used in this system, where $k_{p,imn}$ and $k_{i,imn}$ are the proportional and integral gains, respectively. The feedback control loop for current control, characterized by a plant

$$T(s) = \frac{1}{L_b s + r_b}, \tag{30}$$

is integrated with a PI controller

$$C_b(s) = C_c(s) = k_{p,imn} \frac{s + \frac{k_{i,imn}}{k_{p,imn}}}{s}. \tag{31}$$

This results in a closed-loop equation, which can be compared to a first-order equation,

$$H(s) = \frac{1}{\tau_{imn} s + 1}. \tag{32}$$

17521424, 0, Downloaded from https://ietresearch.onlinelibrary.wiley.com/doi/10.1049/rpg2.12995 by Uppsala University Library, Wiley Online Library on [29/04/2024]. See the Terms and Conditions (https://onlinelibrary.wiley.com/terms-and-conditions) on Wiley Online Library for rules of use; OA articles are governed by the applicable Creative Commons License

TABLE 3 Parameters of the battery controller.

Parameter	Value
Nominal voltage battery	340 V
Switching frequency	25 kHz
L filter	$r_b = 0.03\ \Omega$ and $L_b = 4$ mH
Battery capacity	R.volt = 3.6 V, R.bat = 9 Ah
	Eq.res = 0.12 Ω, N.cells = 95
Current loop gains	$k_{p,ib} = 12.5$ and $k_{i,ib} = 93.75$

TABLE 4 Parameters of the supercapacitor controller.

Parameter	Value
Nominal voltage supercapacitor	300 V
Switching frequency	25 kHz
L filter	$r_c = 0.03\ \Omega$ and $L_b = 4$ mH
supercapacitor capacity	R.volt = 5.5 V, R.cap = 1 F
	Eq.res = 0.5 Ω, N.cells = 55
Current loop gains	$k_{p,ic} = 25$ and $k_{i,ic} = 187.5$
Voltage loop gains	$k_{p,vc} = 6.29$ and $k_{i,vc} = 3.6$

The PI controller gains are calculated as follows:

$$k_{p,imn} = \frac{L_{m,n}}{\tau_{im,in}} \qquad k_{i,imn} = \frac{r_{m,n}}{\tau_{im,in}}. \tag{33}$$

Here, $\tau_{im} = 0.32$ ms and $\tau_{in} = 0.16$ ms. The speed of the current control loops of the battery and the supercapacitor are designed based on their dynamic behaviour according to the switching frequency. Specifically, the battery's current control loop is modelled to be of a slower pace compared to the supercapacitor. This is because of the supercapacitor's faster charge and discharge rates.

2.4.3 | Reference currents estimation

Supercapacitors are primarily used to prevent current spikes from flowing through the batteries. Figure 8 illustrates an outer voltage control loop that regulates the DC-bus link voltage and delivers the current reference I_t^*. This reference is further segregated into two components: a low-frequency component I_{bat}^* which is for the DC/DC converter connected to the batteries, and a high-frequency component I_{sp}^* assigned for the DC/DC converter connected to the supercapacitors. To generate these components, a simple low-pass filter (LPF) is used. The high transient power components are directed towards the supercapacitor, while the battery with greater energy density receives the average component. 50 Hz cut-off frequency for the LPF has been chosen for this study after performing the fast Fourier transform of the input power to the DC-bus. Tables 3 and 4 present the parameter values for the converter, as well as the control gains for the inner and outer loop control.

3 | SIMULATION SETUP

The entire wave-to-grid system has been modelled using MATLAB/Simulink. In this model, the linear generator-based wave energy system takes the wave excitation force as its input. For detailed information about the generator model and the wave-to-wire model, please refer to Dolguntseva et al. [54].

MATLAB/Simulink blocks of diode, IGBT/Diode, battery and supercapacitor are used for the study. Different converters have been designed using the IGBT/Diode blocks, and the control strategies for these components have been discussed in previous sections. Additionally, a three-phase voltage source, representing the grid, is incorporated into the study. The MATLAB/Simulink parameters used for the current study can be seen in Table 5.

TABLE 5 MATLAB/Simulink simulation parameters.

Parameter	Value
Simulation time	5 s
Solver	ode45
Step size	1 μs

Various control modes are employed during specific time intervals to assess the performance of different inverter modes. The objectives include testing the transition time required to achieve a stable state when switching between modes, analyzing voltage behaviour during load fluctuations, evaluating the quality of three-phase voltage and current in various modes, and assessing any impact on power injection into the grid resulting from changes in inverter mode. The activation sequence of these control modes is as follows:

- From 0 to 1 s: grid feeding
- From 1 to 2 s: grid support
- From 2 to 3 s: grid feeding
- From 3 to 4 s: grid forming
- From 4 to 5 s: grid feeding

At the PCC, a three-phase series RLC load with a capacity of 10 kW and 1 kVAR is employed to simulate a load characteristic resembling that of a remote island. Additionally, a 6 kW load is intermittently added at $t = 0.5$ s and $t = 1.5$ s, then removed at $t = 0.75$ s and $t = 2.5$ s. This variation is used to assess the impact on V_{pcc} during different modes and under varying loads.

Furthermore, between 3 s $< t <$ 4 s, the grid is disconnected, and the system operates as an isolated island network. This comprehensive configuration allows for detailed modelling of the entire wave-to-grid system, enabling in-depth analysis of its performance across various scenarios. An illustration depicting the multimode timeslots, various loads, and grid connections is also provided in Figure 9(a).

17521424, 0, Downloaded from https://ietresearch.onlinelibrary.wiley.com/doi/10.1049/rpg2.12995 by Uppsala University Library, Wiley Online Library on [29/04/2024]. See the Terms and Conditions (https://onlinelibrary.wiley.com/terms-and-conditions) on Wiley Online Library for rules of use; OA articles are governed by the applicable Creative Commons License

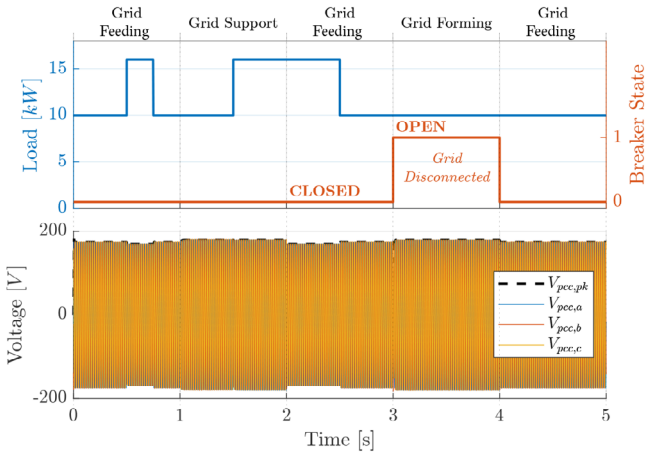

FIGURE 9 Time windows setup and recorded V_{pcc} voltages.

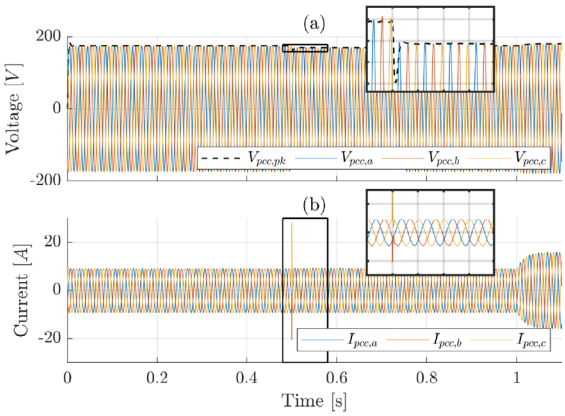

FIGURE 10 PCC voltages (a) and currents (b) during grid feeding mode and an increase in load between $t = 0.5$ s to $t = 0.75$ s.

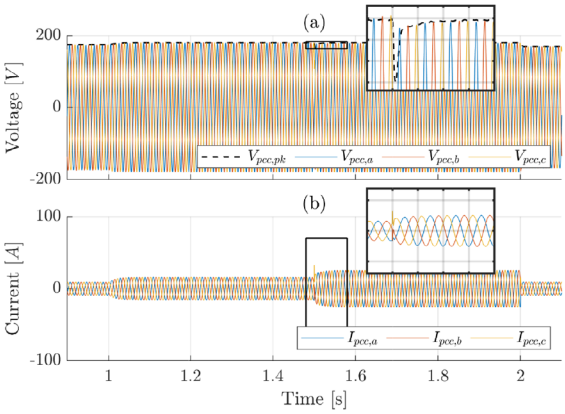

FIGURE 11 PCC voltages (a) and currents (b) during grid support stage.

It is important to highlight that the load has been scaled down to match the capacity of the wave energy system. In practice, the anticipated load for an island is expected to be significantly higher. To comprehensively analyze the energy production of a WEC farm, along with the island's load profile and energy storage dimensioning, a detailed case study is essential, particularly for specific locations which are not addressed in this current study.

4 | RESULTS AND DISCUSSIONS

The simulated results are presented and discussed in this section. In subSection 4.1, Section 4.2 and Section 4.3 the three-phase voltage and current at the PCC during modes 1, 2, and 3 are studied, respectively. Section 4.4 shows the DC-bus voltage, voltage and current of the energy storage for the entire duration. Section 4.5 analyzes the active and reactive powers. Section 4.6 presents the table of the three-phase voltage and current THD for different modes and analyzes the power quality at the PCC.

4.1 | Mode 1: grid-feeding

The three-phase PCC voltage and current during mode 1 are illustrated in Figure 10. It can also be seen from Figure 15 that the voltage at the PCC is lower than 1 pu during this mode. This is due to the losses in the mainland grid connection line, leading to a voltage dip. However, the voltage dip is still inside the range of 0.95 pu, which is the acceptable limit.

During the period from $0.5\,\text{s} < t < 0.75\,\text{s}$, an additional 6 kW load is introduced to the PCC. Notably, this interval experiences a voltage dip to around 0.94 pu. This is attributed to the increased losses in the transmission line. The power flow from the inverter side is still constant at 2 kW during this duration. Hence, the extra power is required from the mainland grid side, leading to higher current, which leads to higher losses. Hence, the increase in load contributes to a decrease in the three-phase AC voltage at the island's PCC. Higher reactive power is required at the PCC to sustain the PCC voltage at its desired level of 1 pu during the higher load scenario. In this case, the voltage decreases below 0.95 pu, which is outside the admissible range of ±5% voltage variation. This voltage dip can be seen in Figure 15, which shows the AC bus voltage for the entire simulation (0–5 s) in pu.

The inverter's current control system effectively delivers the required current to the varying load, as evidenced by Figure 10(b). At $t = 0.75$ s, the additional 6 kW load is removed, resulting in an increase in AC voltage at the PCC. Subsequently, at $t = 1$ s, the inverter control transitions to mode 2.

4.2 | Mode 2: grid-support

At $t = 1$ s, mode 2 is initiated, and the behaviour of the three-phase PCC voltage and current during this mode is depicted in Figure 11. In this mode, the system provides crucial support against voltage dips, effectively raising the AC voltage to the desired level of 1 pu. This desired voltage is maintained through the injection of reactive power by the inverter control. Remarkably, the controller achieves steady-state voltage stabilization within 50 ms.

17521424, 0, Downloaded from https://ietresearch.onlinelibrary.wiley.com/doi/10.1049/rpg2.12995 by Uppsala University Library, Wiley Online Library on [29/04/2024]. See the Terms and Conditions (https://onlinelibrary.wiley.com/terms-and-conditions) on Wiley Online Library for rules of use; OA articles are governed by the applicable Creative Commons License

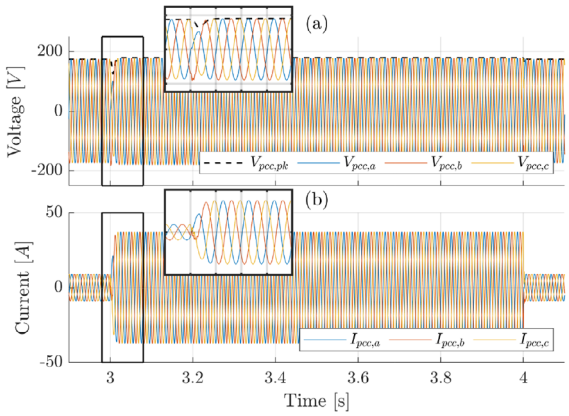

FIGURE 12 PCC voltages (a) and currents (b) during grid forming stage.

During this mode, an additional 6 kW of active load is introduced to the PCC at $t = 1.5$ s, increasing the grid current even further. However, the graph in Figures 11 and 15 reveals that this increase in load does not negatively affect the PCC voltage compared to mode 1. The controller promptly computes a modified iq-current reference value to boost the voltage back to its desired level of 1 pu and injects the required reactive power through the inverter. Even with the increase of the load, the voltage peak at the PCC still remains within the admissible range of ±5% Notably, the system reaches a steady-state condition in just 7 ms.

4.3 | Mode 3: grid-forming

At $t = 3$ s, the grid connection to the WEC, HESS, and island load system is intentionally severed, marking the initiation of mode 3. Figure 12 illustrates the behaviour of the three-phase PCC voltage and current during mode 3. During this mode, the WEC farm, in tandem with the HESS, successfully provides power to satisfy the three-phase load requirements of the island, which is constant at 10 kW and 1 kVAR throughout the entire duration. This uninterrupted supply continues until the grid is reconnected at $t = 4$ s.

Throughout mode 3, the three-phase peak voltage at the PCC consistently maintains the required desired level of 1 pu as evident by Figure 12 and 15. The proposed controller demonstrates its capability to sustain the system's voltage at the specified levels throughout the entire duration of the grid disconnection. Additionally, the system attains a stable state within 19 ms.

4.4 | DC-bus voltage and energy storage

From Figure 13(a), the bus voltage at the DC collection grid is stable during the entire operation of different modes at the required 600 V. The DC-bus voltage has a maximum fluctuation of 2.3 V, which is ±0.38% of the reference voltage, which is inside the acceptable limit of voltage fluctuations of ±5%.

In Figure 13(b), (c), the voltage and current in the battery and supercapacitor can be seen. It is evident from this figure that the

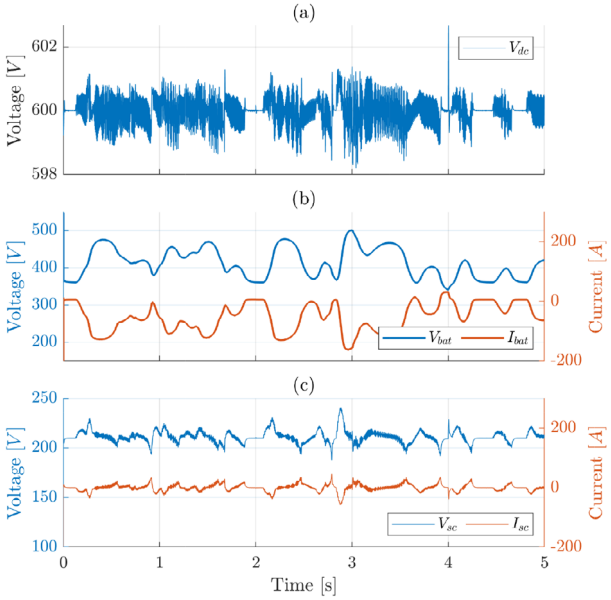

FIGURE 13 DC-bus voltage (a), voltage and current alongside battery (b) and super capacitor (c).

controller is able to reduce the fluctuations in the battery's voltage and current with the help of a supercapacitor. This reduces the stress on the battery by making the high fluctuating charge and discharge currents pass through the supercapacitor. The study related to the quantified impact of using a battery and supercapacitor in a WEC electrical network at the DC-bus can be found in [39] and [29].

4.5 | Powers

Through the power balance analysis on the DC-bus, shown in Figure 14(a), the advantages of the dual energy storage system become evident. As can be seen, the WEC farm inputs power which is oscillatory in both high and low frequencies. The battery is capable of taking advantage of the low-frequency oscillation by constant charging (thus negative delivery), which enables the power injection, albeit shown only briefly right before $t = 4$ s, into the grid during occasions of low generation and grid disconnection. In the meantime, high-frequency oscillations that could increase the battery losses are successfully absorbed by the supercapacitor [29].

The ac side active power balance in Figure 14(b) additionally shows successful supply of the load through constant power during grid feeding ($0\,\text{s} < t < 1\,\text{s}$, $2\,\text{s} < t < 3\,\text{s}$ and $4\,\text{s} < t < 5\,\text{s}$) and grid support ($1\,\text{s} < t < 2\,\text{s}$) modes, as well as full load supply while in grid forming ($3\,\text{s} < t < 4\,\text{s}$).

It should be important to note, however, that the load profile set according to Figure 9 is not accurately reproduced once the weak grid in unable to maintain nominal voltage without grid support. Voltage drops causes the actual power consumption to decrease through $P_{\text{actual}}(t) = P_{\text{nom}} \cdot V_{\text{pu}}^2(t)$, specially at higher power demand.

It is also noteworthy that despite relative constant reactive load, the reactive power flow shown in Figure 14(c) responds

17521424, 0, Downloaded from https://ietresearch.onlinelibrary.wiley.com/doi/10.1049/rpg2.12995 by Uppsala University Library, Wiley Online Library on [29/04/2024]. See the Terms and Conditions (https://onlinelibrary.wiley.com/terms-and-conditions) on Wiley Online Library for rules of use; OA articles are governed by the applicable Creative Commons License

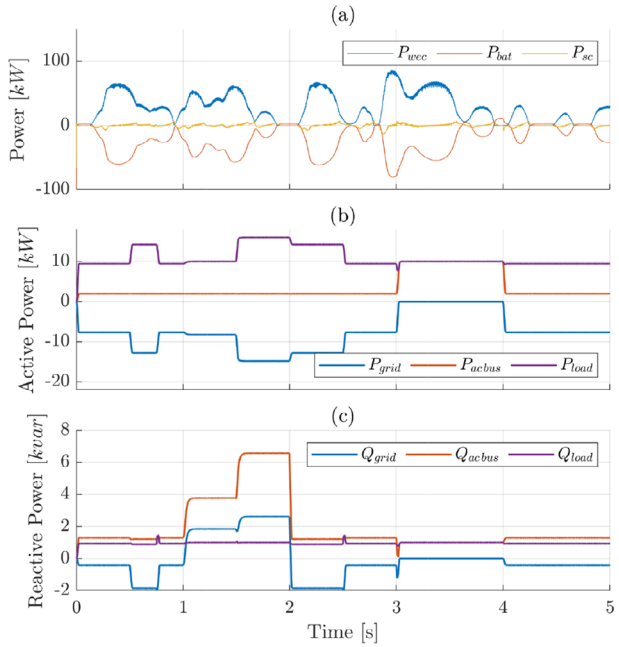

FIGURE 14 Power balance analysis on the DC side (a), as well as active (b) and reactive (b) power flow on the AC side.

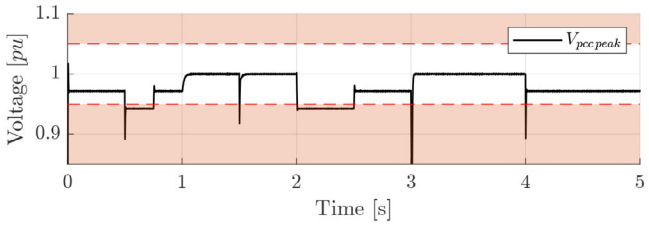

FIGURE 15 Voltage at the PCC in pu.

to increase of active power load once the increase of the grid current over magnetizes the line inductances. This causes the system to drain more reactive power, supplied from the grid. By turning on grid support, however, the inverter injects reactive power, supplying the load and exporting it to the grid, causing the system to return to its nominal value of voltage. This export of reactive power by the inverter can be noted including when the load is increased during grid support mode.

Finally, the PCC voltage is shown in Figure 15. As can be seen, due to the weak grid, the bus is unable to hold nominal voltage without grid support, and the increase of load causes an even higher drop, below the threshold limit. These lower values of voltage explain why the power load profile is not achieved during this step. During grid support, however, voltage is maintained at 1 pu, including during the higher load. The same can be said for grid forming, showing that the inverter is able to keep the island operational at steady conditions.

4.6 | Total harmonic distortion

For all the above modes, the power quality, such as THD of three-phase voltage and three-phase current, is required to be accepted by the TSOs. For it to be accepted, the voltage THD should be within the limit of ±5%. The current THD does not have an absolute limit, as it is expected by a strong grid to suppress the current THD without affecting the grid voltage. However, in the case of weak grid locations such as remote islands, current THD can directly impact the grid voltage THD. On the contrary, the current THD at a grid connection point for a balanced linear load is recommended to be less than ±5%, according to IEEE std 1547 [59, 60]. Hence, for the current study, a current THD limit of ±5% is chosen at the island's load PCC as it is a linear load.

TABLE 6 Voltage THD at the PCC.

Time period	No. of cycles	THD(%)	Fundamental voltage(V)
0-0.5 s (Mode 1)	10	0.38	174.5
0.5-1 s (Mode 1)	10	0.24	169.3
1-1.5 s (Mode 2)	10	0.48	179.6
1.5-2 s (Mode 2)	10	0.23	179.6
3-4 s (Mode 3)	10	0.39	179.6

TABLE 7 Current THD at the PCC.

Time period	No. of cycles	THD(%)	Fundamental current(A)
0-0.5 s (Mode 1)	10	2.23	9.09
0.5-1 s (Mode 1)	10	1.62	9.23
1-1.5 s (Mode 2)	10	1.79	15.83
1.5-2 s (Mode 2)	10	0.66	25.45
3-4 s (Mode 3)	10	0.27	37.29

The analysis does not include the time interval between 2 s $< t <$ 3 s, as well as between 4 s $< t <$ 5 s. This omission is due to the fact that during these periods, the system operates in mode 1, and the data for these intervals matches the analysis of the time interval between 0 s $< t <$ 1 s. All the values are provided in Tables 6 and 7 below.

The THD of the three-phase voltage during different modes at the PCC is given in Table 6. It can be seen that the voltage THD is within acceptable limits during all the modes. It can also be seen that the voltage THD decreases with the addition of 6 kW load demand, which follows the same trend in the current THD, which can be seen in Table 7. With the increment of the load, the fundamental voltage decreases during 0.5 s $< t <$ 0.75 s (mode 1). However, modes 2 and 3 bring back the fundamental voltage to 179.6 V while keeping the THD well within the acceptable level of ±5%.

The THD of the three-phase current during different modes at the PCC is given in Table 7. It can be seen that the current THD is within acceptable limits during all the modes. However, the current THD is reduced by half during the modes 2 and 3 operations, showcasing the improved power quality at the PCC during these modes.

5 | CONCLUSION

This paper introduces a novel approach to a multimode control system for an inverter designed to facilitate the electrification of

17521424, 0, Downloaded from https://ietresearch.onlinelibrary.wiley.com/doi/10.1049/rpg2.12995 by Uppsala University Library, Wiley Online Library on [29/04/2024]. See the Terms and Conditions (https://onlinelibrary.wiley.com/terms-and-conditions) on Wiley Online Library for rules of use; OA articles are governed by the applicable Creative Commons License

an island using a WEC farm in a unified electrified model. Prior research has highlighted the imperative need to electrify islands with renewable energy sources, and in this study, a WEC farm is employed for this purpose. The island's electrical demand is represented by a three-phase load, which draws constant, low-harmonic, active, and reactive power. The power quality at the PCC remains well within acceptable limits of ±5%. The simulation results underscore the necessity of a smart inverter control system during the voltage dip scenario.

The inverter controller presented in this paper guarantees the provision of the required reactive power to correct voltage dips resulting from increased active power drawn from the load. Additionally, it ensures that the inverter maintains system voltage during grid disconnection scenarios, all while continuously supplying power to the island load. The controller is designed to transition seamlessly between these modes, thus enabling island autonomy.

Another noteworthy contribution of this paper pertains to the management of the DC-bus voltage through hybrid energy storage. The DC-bus voltage is regulated to be constant, irrespective of the power generation from the WEC farm. Given the variable and sinusoidally fluctuating nature of wave power, higher-frequency power fluctuations are absorbed by the supercapacitor, while lower-frequency fluctuations are managed by the battery.

AUTHOR CONTRIBUTION

Md Imran Ullah: Conceptualization; investigation; methodology; validation; writing—original draft and editing. **Jessica S. Döhler**: Conceptualization; investigation; methodology; validation; writing—original draft and editing. **Vinicius M. de Albuquerque**: Conceptualization; investigation; methodology; validation; writing—original draft and editing. **Johan Forslund**: Conceptualization; methodology; writing—original draft; editing and supervision. **Cecilia Boström**: Conceptualization; methodology; writing–original draft; editing and supervision. **Irina Temiz**: Conceptualization; methodology; writing—original draft; editing and supervision.

ACKNOWLEDGMENTS

The authors would like to acknowledge the support received from the Department of Electrical Engineering, Uppsala University, Sweden and Standup for Energy, Sweden.

CONFLICTS OF INTEREST STATEMENT

The authors declare no conflicts of interest.

DATA AVAILABILITY STATEMENT

Data sharing is not applicable to this article as no new data were created or analyzed in this study.

ORCID

Md Imran Ullah https://orcid.org/0000-0002-8337-2146
Jessica S. Döhler https://orcid.org/0000-0003-1571-1318

REFERENCES

1. Cross-Call, D.F.: Matching energy storage to small island electricity systems: a case study of the azores. Ph.D. dissertation, Massachusetts Institute of Technology, Cambridge, MA (2013)
2. Asplund, G.: Application of HVDC light to power system enhancement. In: 2000 IEEE Power Engineering Society Winter Meeting. Conference Proceedings, vol. 4, pp. 2498–2503. IEEE, Piscataway, NJ (2000)
3. Singh, G., Baredar, P., Singh, A., Kurup, D.: Optimal sizing and location of PV, wind and battery storage for electrification to an island: a case study of Kavaratti, Lakshadweep. J. Storage Mater. 12, 78–86 (2017). https://www.sciencedirect.com/science/article/pii/S2352152X17301378
4. Keiner, D., Salcedo-Puerto, O., Immonen, E., van Sark, W.G., Nizam, Y., Shadiya, F., Duval, J., Delahaye, T., Gulagi, A., Breyer, C.: Powering an island energy system by offshore floating technologies towards 100% renewables: a case for the Maldives. Appl. Energy 308, 118360 (2022)
5. Alves, M., Segurado, R., Costa, M.: Increasing the penetration of renewable energy sources in isolated islands through the interconnection of their power systems. the case of Pico and Faial islands, Azores. Energy 182, 502–510 (2019)
6. Fadaeenejad, M., Shamsipour, R., Rokni, S., Gomes, C.: New approaches in harnessing wave energy: with special attention to small islands. Renewable Sustainable Energy Rev. 29, 345–354 (2014)
7. Beatty, S.J., Wild, P., Buckham, B.J.: Integration of a wave energy converter into the electricity supply of a remote alaskan island. Renewable Energy 35(6), 1203–1213 (2010)
8. Lee, T., Glick, M.B., Lee, J.-H.: Island energy transition: assessing hawaii's multi-level, policy-driven approach. Renewable Sustainable Energy Rev. 118, 109500 (2020)
9. Falcão, A.F.d.O.: Wave energy utilization: a review of the technologies. Renewable Sustainable Energy Rev. 14(3), 899–918 (2010)
10. Breeze, P.: Marine power generation technologies. In: Power Generation Technologies, 3rd edn. pp. 323–349. Elsevier, Oxford (2019)
11. Gonzalez, A.T., Dunning, P., Howard, I., McKee, K., Wiercigroch, M.: Is wave energy untapped potential? Int. J. Mech. Sci. 205, 106544 (2021)
12. Falnes, J.: A review of wave-energy extraction. Mar. struct. 20(4), 185–201 (2007)
13. Widén, J., Carpman, N., Castellucci, V., Lingfors, D., Olauson, J., Remouit, F., Bergkvist, M., Grabbe, M., Waters, R.: Variability assessment and forecasting of renewables: a review for solar, wind, wave and tidal resources. Renewable Sustainable Energy Rev. 44, 356–375 (2015)
14. Chozas, J.F., Kofoed, J.P., Sørensen, H.C.: Predictability and variability of wave and wind: wave and wind forecasting and diversified energy systems in the Danish North Sea. https://vbn.aau.dk/ws/portalfiles/portal/75674382/Predictability_and_Variability_of_Wave_and_Wind (2013). Accessed 21 August 2023
15. Cornett, A.M.: A global wave energy resource assessment. In: ISOPE International Ocean and Polar Engineering Conference, pp. 1–9. ISOPE, Cupertino, CA (2008)
16. Drew, B., Plummer, A.R., Sahinkaya, M.N.: A review of wave energy converter technology. In: Proc. Inst. Mech. Eng., Part A: J. Power Energy 223(8), 887–1016 (2009)
17. Parwal, A., Remouit, F., Hong, Y., Francisco, F., Castelucci, V., Hai, L., Ulvgård, L., Li, W., Lejerskog, E., Baudoin, A., et al.: Wave energy research at Uppsala University and the Lysekil research site, sweden: a status update. In: Proceedings of the 11th European Wave and Tidal Energy Conference, pp. 08D1-2-1–08D1-2-10. Tethys, Washington, D.C. (2015)
18. Potapenko, T., Burchell, J., Eriksson, S., Temiz, I.: Wave energy converter's slack and stiff connection: study of absorbed power in irregular waves. Energies 14(23), 7892 (2021)
19. Göteman, M., Engström, J., Eriksson, M., Isberg, J., Leijon, M.: Methods of reducing power fluctuations in wave energy parks. J. Renewable Sustainable Energy 6(4), 043103 (2014)
20. Engström, J., Eriksson, M., Göteman, M., Isberg, J., Leijon, M.: Performance of large arrays of point absorbing direct-driven wave energy converters. J. Appl. Phys. 114(20), 204502 (2013)
21. Blavette, A., O'Sullivan, D.L., Lewis, A.W., Egan, M.G.: Impact of a wave farm on its local grid: voltage limits, flicker level and power fluctuations. In: 2012 Oceans-Yeosu, pp. 1–9. IEEE, Piscataway, NJ (2012)
22. Said, H.A., Ringwood, J.V.: Grid integration aspects of wave energy—overview and perspectives. IET Renewable Power Gener. 15(14), 3045–3064 (2021)
23. Kraftnät, S.: Svenska Kraftnät. https://www.svk.se/en/ (2015). Accessed 10 August 2021

17521424, 0, Downloaded from https://ietresearch.onlinelibrary.wiley.com/doi/10.1049/rpg2.12995 by Uppsala University Library, Wiley Online Library on [29/04/2024]. See the Terms and Conditions (https://onlinelibrary.wiley.com/terms-and-conditions) on Wiley Online Library for rules of use; OA articles are governed by the applicable Creative Commons License

24. National Grid ESO: The grid code. https://www.nationalgrideso.com/document/274186/ (2023). Accessed 5 September 2023
25. Power Grid Corporation of India Limited. https://www.powergrid.in/en/company-overview. Accessed 5 September 2023.
26. Etxegarai, A., Eguia, P., Torres, E., Iturregi, A., Valverde, V.: Review of grid connection requirements for generation assets in weak power grids. Renewable Sustainable Energy Rev. 41, 1501–1514 (2015)
27. IEEE Standards Association: IEEE standard for harmonic control in electric power systems. In: IEEE Std 519-2022 (Revision of IEEE Std 519-2014), pp. 1–31. IEEE, Piscataway, NJ (2022)
28. Blavette, A.: Grid integration of wave energy & generic modelling of ocean devices for power system studies. Ph.D. Thesis, University College Cork, Cork (2013)
29. Ullah, M.I., Döhler, J.S., Silva Júnior, D.C., Boström, C., Oliveira, J.G., Temiz, I.: Analysis of a hybrid energy storage system in a grid-tied wave energy converter for varying power demand. In: 11th International Conference on Renewable Power Generation - Meeting Net Zero Carbon (RPG 2022), vol. 2022, pp. 218–222 (2022)
30. Parwal, A., Hjalmarsson, J., Potapenko, T., Anttila, S., Leijon, J., Kelly, J., Temiz, I., de Oliveira, J.G., Boström, C., Leijon, M.: Grid impact and power quality assessment of wave energy parks: different layouts and power penetrations using energy storage. J. Eng. 2021(8), 415–428 (2021)
31. Li, G., Weiss, G., Mueller, M., Townley, S., Belmont, M.R.: Wave energy converter control by wave prediction and dynamic programming. Renewable Energy 48, 392–403 (2012)
32. Sjolte, J., Tjensvoll, G., Molinas, M.: All-electric wave energy converter array with energy storage and reactive power compensation for improved power quality. In: 2012 IEEE Energy Conversion Congress and Exposition (ECCE), pp. 954–961. IEEE, Piscataway, NJ (2012)
33. Neshat, M., Alexander, B., Wagner, M.: A hybrid cooperative co-evolution algorithm framework for optimising power take off and placements of wave energy converters. Inf. Sci. 534, 218–244 (2020)
34. Giassi, M., Göteman, M.: Layout design of wave energy parks by a genetic algorithm. Ocean Eng. 154, 252–261 (2018)
35. Anttila, S., Silva, D., Temiz, I., Oliveira, J.G.d., Leijon, J., Parwal, A., Boström, C.: Power control strategies for a smoother power output from a wave power plant. Paper presented at the 13th European Wave and Tidal Energy Conference (EWTEC), Napoli, Italy, 1–6 September 2019
36. Nie, Z., Xiao, X., Kang, Q., Aggarwal, R., Zhang, H., Yuan, W.: Smes-battery energy storage system for conditioning outputs from direct drive linear wave energy converters. IEEE Trans. Appl. Supercond. 23(3), 5000705 (2013)
37. Murray, D.B., Egan, M., Hayes, J., O'Sullivan, D.: Applications of supercapacitor energy storage for a wave energy converter system. In: EWTEC 2007-7th European Wave and Tidal Energy Conference, pp. 786–795. Tethys, Washington, D.C. (2009)
38. Gao, Q., Ding, B., Ertugrul, N., Li, Y.: Impacts of mechanical energy storage on power generation in wave energy converters for future integration with offshore wind turbine. Ocean Eng. 261, 112136 (2022)
39. Ullah, M.I., Temiz, I., Forslund, J., Döhler, J.S.: Power quality assessment of a wave energy converter using energy storage. Proc. Eur. Wave Tidal Energy Conf. 15, 315 (2023)
40. Boström, C., Lejerskog, E., Stålberg, M., Thorburn, K., Leijon, M.: Experimental results of rectification and filtration from an offshore wave energy system. Renewable Energy 34(5), 1381–1387 (2009)
41. Potapenko, T., Parwal, A., Kelly, J.F., Leijon, J., Hjalmarsson, J., Anttila, S., Boström, C., Temiz, I.: Power hardware in the loop real time modelling using hydrodynamic model of a wave energy converter with linear generator power take off. Paper presented at the ISOPE International Ocean and Polar Engineering Conference, Honolulu,16–21 June 2019
42. Parwal, A., Fregelius, M., Temiz, I., Göteman, M., de Oliveira, J.G., Boström, C., Leijon, M.: Energy management for a grid-connected wave energy park through a hybrid energy storage system. Appl. Energy 231, 399–411 (2018)
43. Sousounis, M.C., Gan, L.K., Kiprakis, A.E., Shek, J.K.: Direct drive wave energy array with offshore energy storage supplying off-grid residential load. IET Renewable Power Gener. 11(9), 1081–1088 (2017)
44. Ullah, M.I., Döhler, J.S., Albuquerque, V., Boström, C., Temiz, I.: Grid-forming control for the linear-generator-based wave energy converter for the electrification of remote islands. In: 12th International Conference on Power Electronics, Machines and Drives (PEMD 2023), pp. 264–270. IEEE, Piscataway, NJ (2023)
45. Curto, D., Favuzza, S., Franzitta, V., Guercio, A., Navia, M.A.N., Telaretti, E., Zizzo, G.: Grid stability improvement using synthetic inertia by battery energy storage systems in small islands. Energy 254, 124456 (2022)
46. Fukaume, S., Nagasaki, Y., Tsuda, M.: Stable power supply of an independent power source for a remote island using a hybrid energy storage system composed of electric and hydrogen energy storage systems. Int. J. Hydrogen Energy 47(29), 13887–13899 (2022)
47. Duarte, S.N., Souza, B.C., Almeida, P.M., Araujo, L.R., Barbosa, P.G.: Control algorithm for DSTATCOM to compensate consumer-generated negative and zero sequence voltage unbalance. Int. J. Electr. Power Energy Syst. 120, 105957 (2020)
48. Anagnostatos, S.D., Halevidis, C.D., Polykrati, A.D., Bourkas, P.D., Karagiannopoulos, C.G.: Examination of the 2006 blackout in Kefallonia island, Greece. Int. J. Electr. Power Energy Syst. 49, 122–127 (2013)
49. Di Silvestre, M., La Cascia, D., Sanseverino, E.R., Zizzo, G.: Improving the energy efficiency of an islanded distribution network using classical and innovative computation methods. Util. Policy 40, 58–66 (2016)
50. Cosentino, V., Favuzza, S., Graditi, G., Ippolito, M.G., Massaro, F., Sanseverino, E.R., Zizzo, G.: Smart renewable generation for an islanded system. technical and economic issues of future scenarios. Energy 39(1), 196–204 (2012)
51. Curto, D., Favuzza, S., Franzitta, V., Musca, R., Navia, M.A.N., Zizzo, G.: Evaluation of the optimal renewable electricity mix for Lampedusa island: the adoption of a technical and economical methodology. J. Cleaner Prod. 263, 121404 (2020)
52. Yazdani, A., Iravani, R.: Voltage-sourced converters in power systems: modeling, control, and applications, 1st edn. Wiley, Hoboken, NJ (2010)
53. Döhler, J.S., Mota, R.P., Archetti, J.A.G., Júnior, D.C.S., Boström, C., Oliveira, J.G.: An application of four-wire grid-forming power inverter in unbalanced distribution network. IET Gener. Transm. Distrib. 17(2), 324–336 (2023)
54. Dolguntseva, I., Eriksson, S., Leijon, M.: Electrical approach to output power control for a point absorbing wave energy converter with a direct drive linear generator power take off. In: Proceedings of the 12th European Wave and Tidal Energy Conference, p. 878-1–878-7. Tethys, Washington, D.C. (2017)
55. Chen, W., Dolguntseva, I., Savin, A., Zhang, Y., Li, W., Svensson, O., Leijon, M.: Numerical modelling of a point-absorbing wave energy converter in irregular and extreme waves. Appl. Ocean Res. 63, 90–105 (2017)
56. Lejerskog, E., Strömstedt, E., Savin, A., Boström, C., Leijon, M.: Study of the operation characteristics of a point absorbing direct driven permanent magnet linear generator deployed in the baltic sea. IET Renewable Power Gener. 10(8), 1204–1210 (2016)
57. Rodríguez, A., Bueno, E.J., Mayor, Á., Rodríguez, F.J., García-Cerrada, A.: Voltage support provided by STATCOM in unbalanced power systems. Energies 7(2), 1003–1026 (2014)
58. Thounthong, P., Rael, S.: The benefits of hybridization. IEEE Ind. Electron. Mag. 3(3), 25–37 (2009)
59. IEEE application guide for IEEE STD 1547(TM), IEEE standard for interconnecting distributed resources with electric power systems. IEEE Std 1547.2-2008, pp. 1–217. IEEE, Piscataway, NJ (2009)
60. Trinh, Q.-N., Lee, H.-H.: An enhanced grid current compensator for grid-connected distributed generation under nonlinear loads and grid voltage distortions. IEEE Trans. Ind. Electron. 61(12), 6528–6537 (2014)

How to cite this article: Ullah, M.I., Döhler, J.S., de Albuquerque, V.M., Forslund, J., Boström, C., Temiz, I.: Multi-mode converter control for linear generator-based wave energy system. IET Renew. Power Gener. 1–15 (2024). https://doi.org/10.1049/rpg2.12995

17521424, 0, Downloaded from https://ietresearch.onlinelibrary.wiley.com/doi/10.1049/rpg2.12995 by Uppsala University Library, Wiley Online Library on [29/04/2024]. See the Terms and Conditions (https://onlinelibrary.wiley.com/terms-and-conditions) on Wiley Online Library for rules of use; OA articles are governed by the applicable Creative Commons License

APPENDIX

The important parameter used to model the three-phase linear generator WEC can be found in Table A1.

TABLE A1 WEC simulation parameters.

Parameter	Value
Buoy type	cylinder
Buoy radius r	1.947 m
Buoy height h	1.05 m
Buoy draft d	0.64 m
Mass of buoy m_b	3000 kg
Buoy moment of Inertia I_b	6000 kg.m^2
Water depth D	25 m
Mass of translator m_t	5000 kg
Length of translator l_t	2132 m
Length of stator l_s	1.199 m
End stop spring coefficients k_s	270 kN/m
Wire rope spring coefficients k_w	833 kN/m
Free stroke length l_f	0.622 m
Maximum stroke length upwards l_u	1.612 m
Maximum stroke length downwards l_l	1.106 m
Distance between the case and buoy's CoG L_0	14.6 m
Rated translator speed v_n	0.7 m/s
Pole pair width τ_p	79.5 mm
Induced voltage (emf, $l-l$, rms) E_{l-l}	257 V
Generator resistance R_g	0.64 Ω
Generator inductance L_g	20 mH
Generator losses damping force F_{loss}	1 kN

17521424, 0, Downloaded from https://ietresearch.onlinelibrary.wiley.com/doi/10.1049/rpg2.12995 by Uppsala University Library, Wiley Online Library on [29/04/2024]. See the Terms and Conditions (https://onlinelibrary.wiley.com/terms-and-conditions) on Wiley Online Library for rules of use; OA articles are governed by the applicable Creative Commons License